energies

MDPI

Article

Numerical Simulation of a 10 kW Gas-Fueled Chemical Looping Combustion Unit

Liyan Sun *, Junjie Lin, Dali Kong, Kun Luo and Jianren Fan

State Key Laboratory of Clean Energy Utilization, Zhejiang University, Hangzhou 310058, China; linjunjie@zju.edu.cn (J.L.); dalikong@zju.edu.cn (D.K.); zjulk@zju.edu.cn (K.L.); fanjr@zju.edu.cn (J.F.)
* Correspondence: sunliyan@zju.edu.cn

Abstract: Chemical looping combustion is one novel technology for controlling CO_2 emission with a low energy cost. Due to a lack of understanding of the detailed and micro behavior of the CLC process, especially for a three dimensional structure, numerical simulations are carried out in this work. The configuration is built according to the experimental unit and gaseous fuel is used in this work. A two-fluid model considering heterogeneous reactions is established, and the flow behaviour and reaction characteristics are obtained. The temperature in the air reactor increases with height owing to the exothermic reaction of the xidation of the oxygen carrier, while the temperature in the fuel reactor decreases with height due to the endothermic reaction. The oxidation level of the oxygen carrier is obtained by simulation, which is hard for measurement, and the difference between the inlet and outlet is 0.065. The influences of the operating temperature and injection rate of fuel are presented to understand the performance of the system. The highest fuel conversion rate reaches 0.92 under high operating temperature. The numerical results are helpful for acquiring insight on the flow and reactive behaviour of CLC reactors.

Keywords: CLC; circulating fluidized bed; numerical simulation

Citation: Sun, L.; Lin, J.; Kong, D.; Luo, K.; Fan, J. Numerical Simulation of a 10 kW Gas-Fueled Chemical Looping Combustion Unit. *Energies* **2022**, *15*, 1973. https://doi.org/10.3390/en15061973

Academic Editor: Maria Cristina Cameretti

Received: 24 January 2022
Accepted: 2 March 2022
Published: 8 March 2022

1. Introduction

Chemical looping combustion is one of the technologies used for carbon dioxide capture, which is beneficial for controlling the impact of greenhouse gas on the climate and on the increase in global temperature [1,2]. This technology provides an alternative method to producing high concentration CO_2 exhaust, with the reactions isolated into two separated reactors. An oxygen carrier transports lattice oxygen and heat between reactors, as a result the air never mixes with the combustion products. The pure CO_2 is obtained after condensing the products of the fuel reactor with less energy for gaseous separation [3]. The net reaction, mass transfer and heat release of CLC are similar to the traditional method of fuel combustion. The difference is that no penalty energy is needed for CO_2 separation. The CLC technology exhibits an obvious advantage for CO_2 capture with low energy cost [4,5].

The typical configuration of a CLC system consists of a fuel reactor, air reactor and loop seals. The diagram for the CLC system is shown in Figure 1. The experiments for the CLC system with dual interconnected fluidized reactors have been successfully carried out at lab scale and pilot scale, with both gaseous fuel and solid fuel [6–8], coal [7,9], petroleum [10], biomass [11] and liquid fuel [12], which prove the feasibility of the CLC technology. At the same, researchers have used the numerical method to investigate the operating behaviour of the CLC system, which is difficult for experimental measurement [13,14], and it has played a more and more important role for investigating the CLC system [15–17]. Two main methods, two-fluid model and discrete element method (DEM), are utilized for simulating the CLC system [18–20]. With DEM, one can track the trajectory of each particle and get the information at particle scale. Kong et al. [21] simulated the CLC system using DEM and

the effect of PSD(particle size distribution) on the conversion of fuel conversion. Results showed the positive impact on the performance of the reactor. Lin et al. [22] investigated the CLC system with a dual interconnected reactor using DEM. The residence time can be counted and analysed, and the results provided the particle scale understanding of the operation. The disadvantage of DEM is that the computational cost is huge with the increase in particles in the system. Currently, DEM is not possible for the large scale reactor, especially at a pilot or industrial scale. For the two-fluid model, both the gas phase and solid phase are treated as interpenetrating continua and it obtains considerable calculation speed. Chen et al. [18] utilised a two-fluid model to study the bubble behaviour in a fuel reactor. Francisco et al. [23] developed the model for analysing the 1D fuel reactor. The results show that a higher temperature was desired for high carbon capture, but had a smaller effect on oxygen demand. The carbon capture efficiency increased to 98.6% when raising the temperature to 1100 °C and with a carbon separation efficiency 98%. Kavitha et al. [24] carried out a 2D simulation of a fuel reactor with coal as fuel. When considering ash during simulations, the performance of CuO and Fe_2O_3 were thesame, if no ash, the CuO performed better. The char gasification was the limited step of the CLC process. Wang et al. [25] pointed out that the formation of large bubbles lead to low fuel conversion. May [26] simulated the 3D CLC system using coal without the cyclone and loop-seal, instead of the changing mass flow rate at the boundary. The utilization of a drag model lead to deviation between the predictions and measurements, especially for the reaction with a different flow regime. Li et al. [27] carried out the 3D simulation of cold flow for hydrodynamic analysis. The full loop structure was constructed. The nonuniformity of flow behavior was observed. Wall roughness showed the indefinite affect and tendency. To sum up, according to the literature review, the fundamental mechanism of the operation of CLC has been investigated through both experiments and theoretical methods, in order to maximize the fuel conversion and carbon capture. However, there are few studies that focus on the full loop CLC system, and the coupling between reactors are missing. Moreover, three dimensional numerical structure is essential to reveal the properties of operation, but currently most works are on the two dimensional structure and only hydrodynamics research. Operating details are needed for which are difficult for experiments.

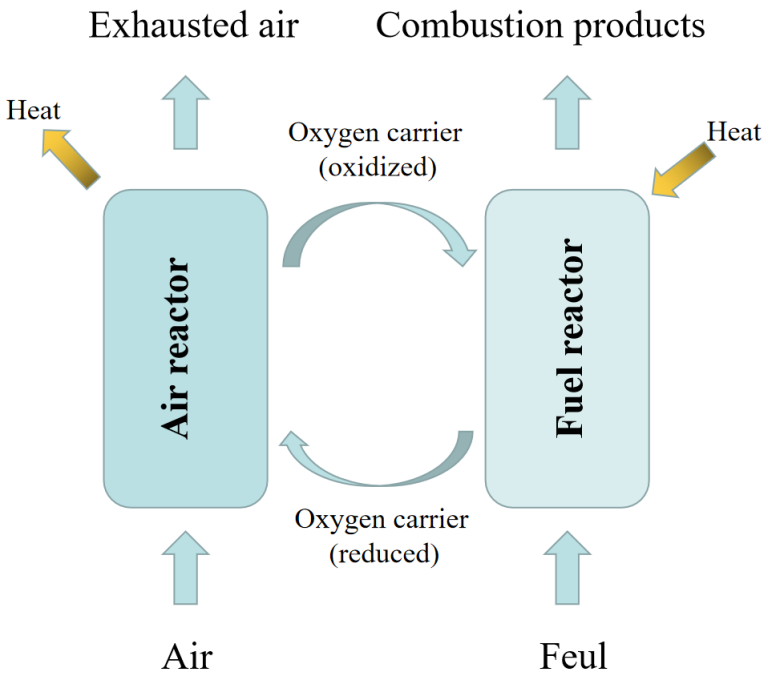

Figure 1. Schematic of chemical looping combustion system.

To overcome this insufficiency, in this work, a two-fluid model for a full loop three dimensional gas-fueled chemical looping system is developed for exploring the flow and reaction behavior. The CLC geometry is constructed according to the experiment one consisting of two interconnected reactors, cyclone and loop seal. The literature review shows that there is very little research relating to the circulation behaviour and reaction characteristics in full loop structures. The motivation of the current work is to gain the operating behavior of the three dimensional CLC unit at a micro-scale. The data obtained from simulations will be helpful for designing and operating the CLC system.

2. Mathematical Models

A two-fluid model is utilised for modeling the transport equation of mass, momentum, energy and species. The kinetic theory of granular flow is adopted for the closure of the solid phase. The transport equations solved in this work are shown in Tables A1 and A2 in the Appendix A, which has been tested in our previous works [22,28,29]. The fuel used in current work is methane and the reactions of oxygen carrier are following

$$12Fe_2O_3 + CH_4 \rightarrow 8Fe_3O_4 + CO_2 + 2\,H_2O$$
$$4Fe_3O_4 + O_2 \rightarrow 6Fe_2O_3$$

The reaction process is described by the changing grain size model [30,31]. Considering the effect of reaction kinetics, the reaction procedure is described as the following:

$$\frac{t}{\tau_{chr}} = 1 - (1 - X_i)^{1/3} \quad (1)$$

$$\tau_{chr} = \frac{\rho_m r_g}{\bar{b} k_s C_g^n} \quad (2)$$

where X_i presents the conversion rate and τ_{chr} presents the corresponding time, which can be calculated based on Table 1 [30].

Table 1. Kinetic parameters for reduction and oxidation of oxygen carriers.

ρ_m (mol m $^{-3}$)	r_g	$\bar{b}$	k_{s0} (mol^{1-n}m^{3n-2}s^{-1})	E_{chr} (kJ mol^{-1})	n
13,590	1.25×10^{-6}	5.78	9.8	135.2 ± 6	1

The conversion rate, X_i, is defined as

$$X_r = \frac{m_o - m}{R_{o,ilm} m_o} \quad (3)$$

where $R_{o,ilm}$ represents the oxygen transport capacity. The homogeneous reactions, $CH_4 + 2O_2 \rightarrow CO_2 + 2H_2O$, is considered is this work with the reaction rate $\frac{d[CH_4]}{dt} = -k[CH_4]^{0.7}[O_2]^{0.8}$, $k = 1.580 \times 10^{23} exp\left(-\frac{24343}{T_g}\right)$ [32].

3. Simulation Setup

A chemical looping combustion system with dual interconnected reactors, as shown in Figure 2, is adopted to investigate the reactive characteristics and hydrodynamic behaviour. It consists of an air reactor, fuel reactor, cyclone and loop seal. The configuration used here is built according to the work of Johansson et al. [33] and Guann et al. [34]. The total height is 1.9 m. The diameter is 0.19 m for both air reactor and fuel reactor. $k - \varepsilon$ model is adopted for simulating gas turbulence. A non slip boundary condition is set for the wall. The methane is similarly adopted to the experiment and ilmenite is utilized as the oxygen carrier. More information about the numerical method can be found in our previously published works [28,35].

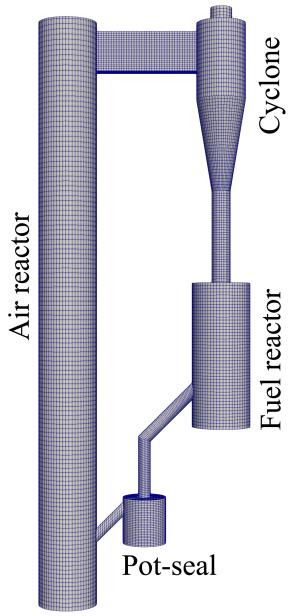

Figure 2. Geometry of CLC system. The amount of cell is 0.33 million.

4. Results and Discussion

4.1. Flow Behavior of CLC System

The profile of instantaneous distribution of solid volume fraction is displayed in Figure 3. The particles circulate between reactors to exchange the lattice oxygen. Initially, the particles are located at the bottom of air reactor, fuel reactorand the loop seal. When the fluidizing gas is introduced to the reactor, the particles switch to the fluidizing state and different flow regime can be found in the CLC system. The particles in AR are entrained by gas phase and flow out of the riser, then they are separated by cyclone and enter FR. With the loop seal, particles will be sent back to AR and realize the circulation. Here, the loop seal works with a low velocity for preventing the exchange between AR and FR, which is prohibited for CLC system. The corresponding flow rate of the oxygen carrier is shown in Figure 4. The measured position is near the outlet of riser. The flow rate fluctuates with the time which is caused by the formation and breakup of bubbles and the interaction between gas and solid. After 35 s, the reactors tend to be steady state, so the solid flow rate of AR is equal to FR, and to the loop seal. Additionally, the solid flow rate is hard to measure during the experiment, while we can get it from the simulation. Under current conditions, the solid circulating rate is about 0.4 kg/s.

4.2. Reaction Behavior of CLC System

Figure 5 shows the profile of the gas species mass fraction at the outlets of AR and FR with the inlet rate of methane 0.5 g/s with temperature 200 °C. The total solid inventory of the oxygen carrier is 34.6 kg. At the initial time, some methane crosses the bed materials due to the insufficient oxygen carrier. After 40s, the mass fraction of gaseous species reaches a steady value and the particles have shifted from air reactor to the fuel reactor for the balance of mass. The methane is not fully converted under current conditions. The main products detected at the outlet of the fuel reactor are CO_2 and H_2O. In the air reactor, the oxygen is consumed by the oxidation of oxygen carrier, and this value is equal to the consumption of oxygen in the fuel reactor. Much less CO_2 is found in the air reactor due to leakage of the gas from loop seal.

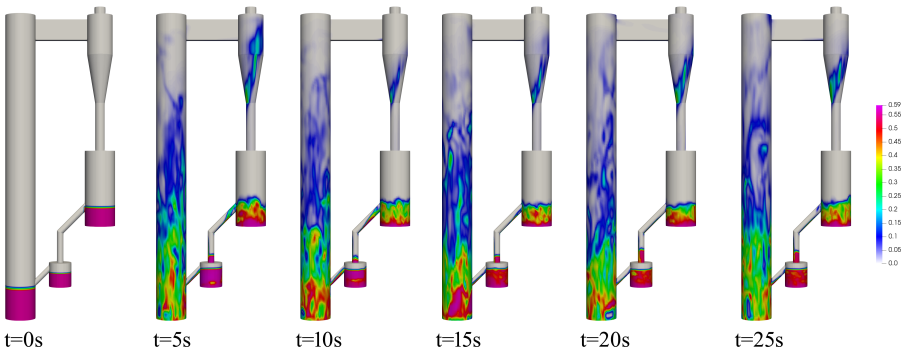

Figure 3. Flow pattern of solid phase in CLC reactor.

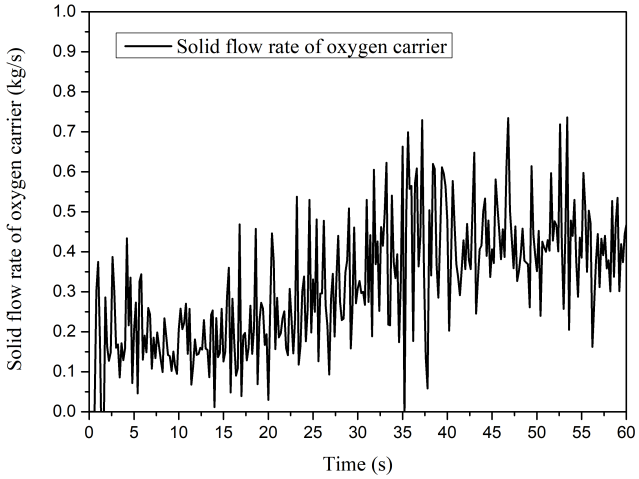

Figure 4. Time-evolution of solid flow rate of oxygen carrier. The solid inventory is 34.6 kg.

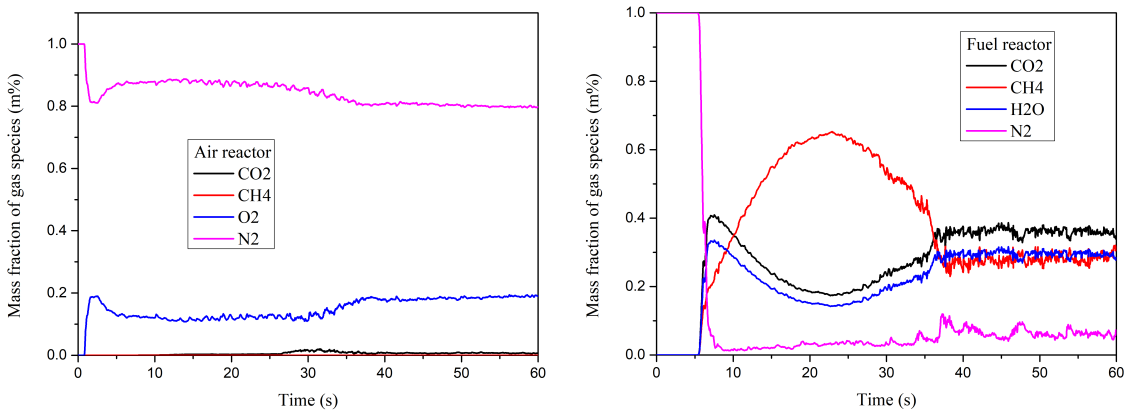

Figure 5. Time-evolution of mass fraction of gas species. The inlet rate of methane is 0.5 g/s.

The distribution of temperature in both AR and FR is shown in Figure 6. In AR, the oxygen carrier reacts with oxygen, which is an exothermic process. In FR, the reduction of the oxygen carrier is an endothermic process. As shown in Figure 6, the temperature in AR is low at the bottom due to the injection of air with a low temperature. Then, the temperature increases because of the heat transfer between oxygen carrier and gas phase. The decrease in temperature at a height of 0.3 m is caused by the inlet of the loop seal, where the cold gas and particles are injected into the air reactor. Then, temperature keeps increasing due to the reaction heat releasing during the oxidation process of oxygen carrier. At the bottom of FR, the temperature is high because oxygen carriers from the air reactor

with high temperature enter FR. The temperature decreases with height and it is nearly constant (957K) at the end of the reactor. The distribution of temperature in the system is consistent with the theoretical analysis. We get a similar trend of temperature as in the work of Want et al. [17] on a CLC simulation.

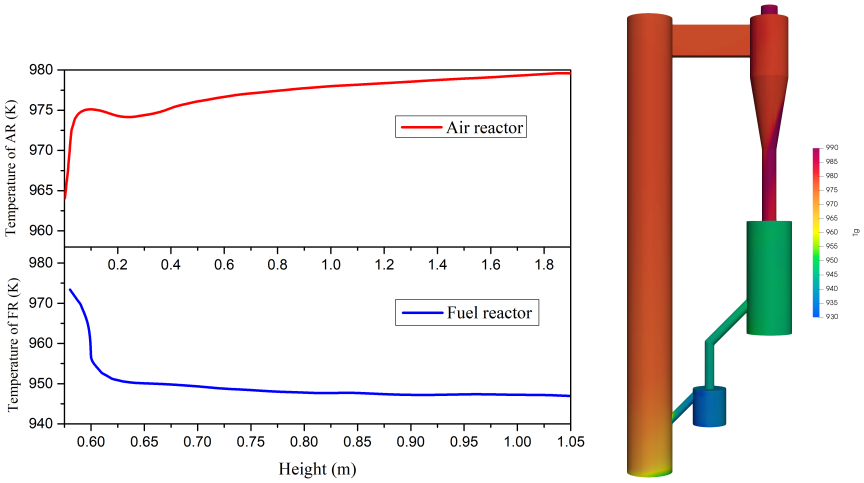

Figure 6. Distribution of temperature in the CLC system. **Left**: Profile of time-averaged temperature in AR and FR. **Right**: Plot of gas phase temperature in the system.

To assess the state of the oxygen carrier, the oxidation level is calculated at the inlet and outlet of AR and shown in Figure 7. The difference between the two curves reflects the oxygen transfer between AR and FR, also the oxygen consumption in the fuel reactor. These values are the same with the outlet and inlet value of the fuel reactor, since the reactors are connected. Initially, fully reduced particles fill the loop seal for maintaining the temperature of the system. So, the oxidation level is low at the inlet of the air reactor at the beginning. After 30 s, the system becomes steady and the oxidation level is around 0.935 at the inlet of the AR. In fact, the oxidation level is decided by the reaction of the oxygen carrier in FR. For the outlet of the air reactor, the oxidation level is about 1, and the oxygen carrier has been fully oxidized. Based on the solid circulating rate and the conversion rate of methane, we can calculate the theoretical oxidation level, as shown in Figure 7 in blue. The simulated result is close to the theoretical one. Moreover, we find that the oxidation of the oxygen carrier is fast and the reduction process is the limitation of system.

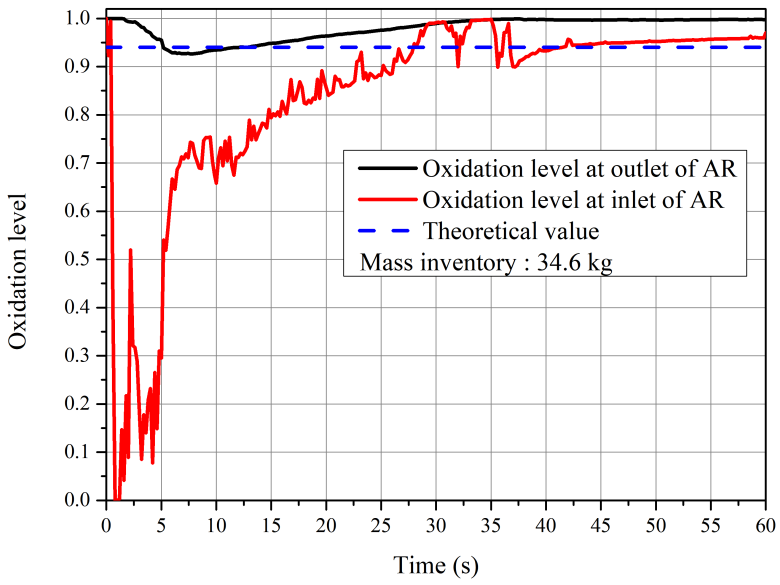

Figure 7. Time evolution of oxidation level. The solid inventory is 34.6 kg.

4.3. Influence of Fuel Inlet Rate

The influence of the inlet rate of methane is tested, which corresponds to the CO_2 capture capacity of the system. The mass fraction of gaseous species at the outlet of the FR are shown in Figure 8 for three cases with an inlet rate of 0.25 g/s, 0.5 g/s and 1.0 g/s. The CO_2 fraction decreases with the methane inlet rate and the same tendency for the water vapour. Additionally, more methane is found at the FR outlet, because of the short contact time between gas and oxygen carrier. The corresponding distribution of gas species is illustrated in Figure 9. It shows intuitively the variety of the product and reactant with inlet rate. We can find CO_2 in the loop seal and air reactor, which is caused by the leakage and is quite low in this work. The results are consistent with the work of Johansson [33].

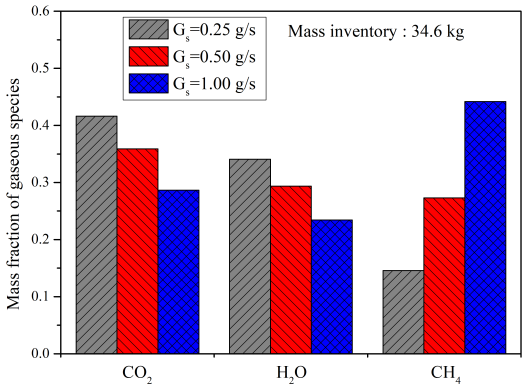

Figure 8. Time-averaged gaseous mass fraction at the outlet of fuel reactor. The solid inventory is 34.6 kg.

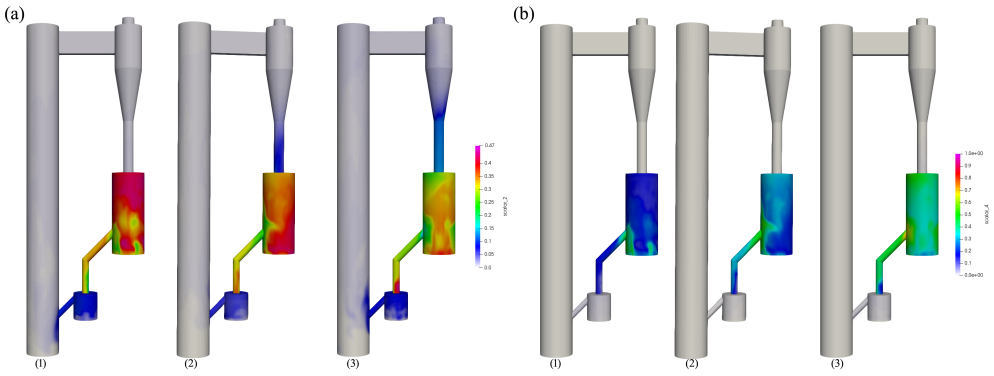

Figure 9. Instantaneous distribution of gas species with different inlet rate of methane. (**a**) CO_2. (**b**) CH_4. (1) 0.25 g/s. (2) 0.5 g/s. (3) 1.0 g/s.

The performance of CLC can be assessed by fuel conversion rate, which is defended as following [36],

$$X_{CH_4} = \frac{F_{in,CH_4} - F_{out,CH_4}}{F_{in,CH_4}} \tag{4}$$

The carbon capture efficiency used in this work is defined as following [37],

$$\eta_{cc} = \frac{F_{FR,CO_2} - F_{AR,CO_2}}{F_{in,CH_4}} \tag{5}$$

From Figure 10, the conversion rate decreases with the methane injection rate, also less methane is converted into CO_2 under current conditions. The resistance time decreases when increasing the FR inlet rate. Under current conditions, the operating temperature of FR is about 940 K and the total mass inventory is 34.6 kg, it is hard for the system to convert more methane and most of it escapes the reactor. The capture efficiency is quite

low with a high inlet rate of methane. One possible solution is to increase the inventory or the operating temperature.

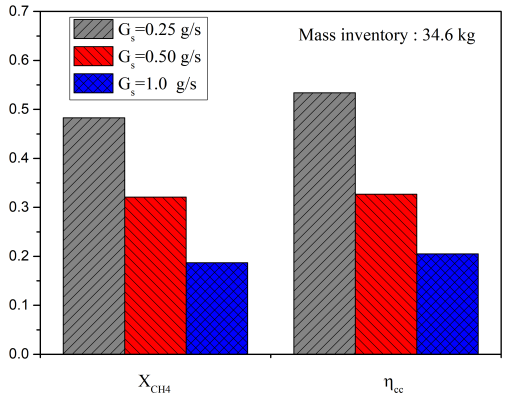

Figure 10. Time-averaged conversion rate CH4 and CO_2 capture efficiency of fuel reactor under different inlet rate. The solid inventory is 34.6 kg.

4.4. Influence of Operating Temperature

The performance of the CLC system under different temperatures is analysed in this section. As shown in Figure 11, the mass fraction of CH_4 at the FR outlet decreases with temperature, which is due to the kinetic reaction increasing with temperature. More products, CO_2 and H_2O, are generated simultaneously. The nitrogen is also detected at FR outlet, which is from the loop seal. The conversion of fuel is an important parameter to assess the CLC performance. As shown on the right of Figure 11, the conversion rate of methane increases from 0.33 to 0.92 when raising the operating temperature from 930 K to 1290 K. The relationship is approximately linear, with a slope of 0.0024 per Kelvin. The oxygen demanded is the fraction of O_2 required to fully burn the fuel and O_2 needed by the unconverted gas exiting FR [38]. The similar effect of temperature has been presented in the work of Liu et al. [39]. From the figure, the oxygen demanded decreases with temperature, because more methane has been converted in FR with a higher temperature. Under current conditions, high operating temperature is beneficial for improving the performance of system.

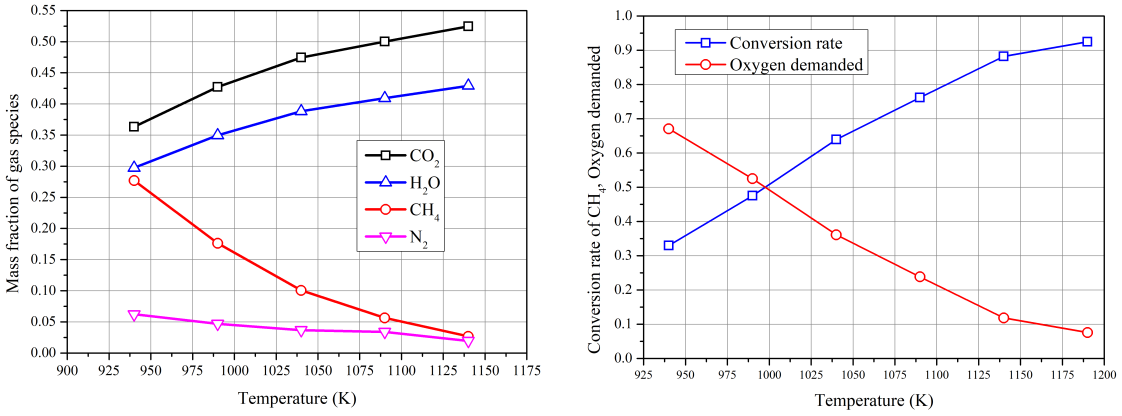

Figure 11. Effect of temperature on the performance of system. **Left**: gaseous mass fraction at FR outlet. **Right**: Conversion rate of methane and outlet rate of fuel reactor.

5. Conclusions

A 3D model for a full loop CLC system is built in the frame of the Eulerican-Eurlerian approach for investigating the operation of a 10 kW gas-fueled CLC system. The temperature increases with height in the air reactor, due to the exothermic oxidation process of the oxygen carrier, and the temperature in the fuel reactor decreases slightly due to

the reduction of oxygen carrier being a endothermic process. The temperature difference between reactors is 24 K The oxidation level is calculated during the simulation, which is difficult in the experiment. The difference in oxidation levels between the inlet and outlet of the air reactor is about 0.065, which is consistent with the theoretical value. The higher injection rate of methane will lead to a lower fuel conversion rate, due to the short resistance time and interaction time between the gas and oxygen carrier. The carbon capture efficiency decreases from 0.54 to 0.2 when the gas flow rate increases from 0.5 g/s to 1.0 g/s The operating temperature is an essential parameter for the performance of the CLC system. Under certain cases, the conversion rate of methane reaches 0.92 when raising the operating temperature to 1290 K. The industrial simulations will be carried out in following research based on the current work.

Author Contributions: Conceptualization, L.S. and K.L.; methodology, L.S., D.K. and J.L.; software, L.S., J.L. and D.K.; validation, L.S., K.L. and J.F.; writing—review and editing, L.S., K.L. and J.F.; supervision, J.F. All authors have read and agreed to the published version of the manuscript.

Funding: This research was funded by National Key Research and Development Plan (No. 2017YF E0112500) and National Natural Science Foundation of China (No. 51806192, 51925603).

Institutional Review Board Statement: Not applicable.

Informed Consent Statement: Not applicable.

Data Availability Statement: Data available in a publicly accessible repository.

Conflicts of Interest: The authors declare no conflict of interest.

Appendix A

Table A1. Transport equation.

	Mass balance equation
T1	$\frac{\partial(\alpha_g\rho_g)}{\partial t}+\frac{\partial(\alpha_g\rho_g U_{g,j})}{\partial x_j}=\Gamma_g$
T2	$\frac{\partial(\alpha_s\rho_s)}{\partial t}+\frac{\partial(\alpha_s\rho_s U_{s,j})}{\partial x_j}=\Gamma_s$
	Momentum equation
T3	$\frac{\partial\alpha_g\rho_g\mathbf{u}_g}{\partial t}+\bigtriangledown\cdot(\alpha_g\rho_g\mathbf{u}_g\mathbf{u}_g)=-\alpha_g\bigtriangledown p+\bigtriangledown\cdot(\alpha_g\tau_g)+\alpha_g\rho_g\mathbf{g}+\beta(\mathbf{u}_s-\mathbf{u}_g)$
T4	$\frac{\partial\alpha_s\rho_s\mathbf{u}_s}{\partial t}+\bigtriangledown\cdot(\alpha_s\rho_s\mathbf{u}_s\mathbf{u}_s)=-\alpha_s\bigtriangledown p+\bigtriangledown\cdot(\alpha_s\tau_s)+\alpha_s\rho_s\mathbf{g}+\beta(\mathbf{u}_g-\mathbf{u}_s)$
	k-ε model
T5	$\frac{\partial}{\partial t}(\alpha_g\rho_g k)+\bigtriangledown\cdot(\alpha_g\rho_g u_g k)=\bigtriangledown\cdot\left(\alpha_g\frac{\mu_t}{\sigma_k}\bigtriangledown k\right)+\alpha_g G_k-\alpha_g\rho_g\varepsilon$
T6	$\frac{\partial}{\partial t}(\alpha_g\rho_g\varepsilon)+\bigtriangledown\cdot(\alpha_g\rho_g u_g\varepsilon)=\bigtriangledown\cdot\left(\alpha_g\frac{\mu_t}{\sigma_\varepsilon}\bigtriangledown\varepsilon\right)+\alpha_g\frac{\varepsilon}{k}(C_1G_K-C_2\rho_g\varepsilon)-\alpha_g\rho_g\varepsilon$
	Transport equation of granular temperature
T7	$\frac{3}{2}\left[\frac{\partial}{\partial t}(\alpha_s\rho_s\theta)+\bigtriangledown\cdot(\alpha_s\rho_s\theta)u_s\right]=(-\bigtriangledown p_s\mathbf{I}+\tau_s):\bigtriangledown u_s+\bigtriangledown\cdot(k_s\bigtriangledown\theta)-\gamma_s-3\beta\theta+D_{gs}$
	Species transport equation
T8	$\frac{\partial\alpha_g\rho_g Y_{g,i}}{\partial t}+\bigtriangledown\cdot(\alpha_g\rho_g\mathbf{u}_g Y_{g,i})=\bigtriangledown\cdot(\alpha_g J_{g,i})+S_{g,i}$
T9	$\frac{\partial\alpha_s\rho_s Y_{s,i}}{\partial t}+\bigtriangledown\cdot(\alpha_s\rho_s\mathbf{u}_s Y_{s,i})=\bigtriangledown\cdot(\alpha_s J_{s,i})+S_{S,i}$
	Transport equation of enthalpy
T10	$\frac{\partial}{\partial t}(\alpha_g\rho_g H_g)+\bigtriangledown\cdot(\alpha_g\rho_g\mathbf{u}_g H_g)=\bigtriangledown(\kappa_g\bigtriangledown T_g)+h(T_g-T_s)+\varphi_g$
T11	$\frac{\partial}{\partial t}(\alpha_s\rho_s H_s)+\bigtriangledown\cdot(\alpha_s\rho_s\mathbf{u}_s H_s)=\bigtriangledown(\kappa_s\bigtriangledown T_s)+h(T_s-T_g)+\varphi$

Table A2. Conservation equation.

	Stress tensor
C1	$\tau_g = \mu_g[\nabla \mathbf{u}_g + (\nabla \mathbf{u}_g)^T] - \frac{2}{3}\mu_g(\nabla \cdot \mathbf{u}_g)I$
C2	$\tau_s = \mu_s[\nabla \mathbf{u}_s + (\nabla \mathbf{u}_s)^T] - (\lambda_s - \frac{2}{3}\mu_s)(\nabla \cdot \mathbf{u}_s)I$
	Interphase momentum transfer coefficient
C3	$\beta = \begin{cases} \frac{3}{4}\left(\frac{C_D \alpha_g \alpha_s \rho_g \lvert \mathbf{u}_g - \mathbf{u}_s \rvert}{d_s}\right)\alpha_s^{-2.65} & \alpha_s < 0.2 \\ 150\left(\frac{\mu_g \alpha_s^2}{\alpha_s d_s^2}\right) + 1.75\left(\frac{\alpha_s \rho_g}{d_s}\right)\lvert \mathbf{u}_g - \mathbf{u}_s \rvert & \alpha_s \geq 0.2 \end{cases}$
C4	$C_D = \begin{cases} \frac{24}{R_e \alpha_g}\left[1 + 0.15(R_e \alpha_g)^{0.687}\right] & R_e < 1000 \\ 0.44 & R_e \geq 1000 \end{cases}$
C5	$R_e = \frac{\rho_g d_s \lvert \mathbf{u}_g - \mathbf{u}_s \rvert}{\mu_g}$
	shear viscosity
C6	$\mu_g = C_\mu \frac{k^2}{\varepsilon}$
C7	$\mu_s = \frac{4}{5}\alpha_s^2 \rho_s d_s g_0 (1+e)\sqrt{\frac{\theta}{\pi}} + \frac{10\rho_s d_s \sqrt{\pi\theta}}{96(1+e)\alpha_s g_0}\left[1 + \frac{4}{5}g_0 \alpha_s (1+e)\right]^2$
	Solid pressure
C8	$p_s = \alpha_s \rho_s \theta + 2\rho_s (1+e)\alpha_s^2 g_0 \theta$
	Conductivity of fluctuating energy
C9	$k_s = \frac{25\rho_s d_s \sqrt{\pi\theta}}{64(1+e)g_0}\left[1 + \frac{6}{5}(1+e)g_s \alpha_s\right]^2 + 2\alpha_s^2 \rho_s d_s g_0 (1+e)(\frac{\theta}{\pi})^{1/2}$
	Dissipation rate of fluctuating energy
C10	$\gamma_s = 3(1-e^2)\alpha_s^2 \rho_s g_0 \theta\left(\frac{4}{d_s}\sqrt{\frac{\theta}{\pi}} - \nabla \cdot u_s\right)$
	Heat transfer coefficient
C11	$h = \frac{6\alpha_s \alpha_g \lambda_g Nu}{d_p^2}$
C12	$Nu = (7 - 10\alpha_g + 5\alpha_g^2)(1 + 0.7Re^{0.2}Pr^{1/3}) + (1.33 - 2.4\alpha_g + 1.2\alpha_g^2)Re^{0.7}Pr^{1/3}$
C13	$Pr = \frac{\mu_g C_g}{\lambda_g}$

References

1. Saqline, S.; Chua, Z.Y.; Liu, W. Coupling chemical looping combustion of solid fuels with advanced steam cycles for CO_2 capture: A process modelling study. *Energy Convers. Manag.* **2021**, *244*, 114455. [CrossRef]
2. Bui, M.; Adjiman, C.S.; Bardow, A.; Anthony, E.J.; Boston, A.; Brown, S.; Fennell, P.S.; Fuss, S.; Galindo, A.; Hackett, L.A.; et al. Carbon capture and storage (CCS): The way forward. *Energy Environ. Sci.* **2018**, *11*, 1062–1176. [CrossRef]
3. Abad, A.; Mattisson, T.; Lyngfelt, A.; Rydén, M. Chemical-looping combustion in a 300W continuously operating reactor system using a manganese-based oxygen carrier. *Fuel* **2006**, *85*, 1174–1185. [CrossRef]
4. Ishida, M.; Zheng, D.; Akehata, T. Evaluation of a chemical-looping-combustion power-generation system by graphic exergy analysis. *Energy* **1987**, *12*, 147–154. [CrossRef]
5. Chein, R.Y.; Chen, W.H. Thermodynamic analysis of integrated adiabatic chemical looping combustion and supercritical CO_2 cycle. *Energy Convers. Manag. X* **2021**, *10*, 100078. [CrossRef]
6. Abad, A.; Mattisson, T.; Lyngfelt, A.; Johansson, M. The use of iron oxide as oxygen carrier in a chemical-looping reactor. *Fuel* **2007**, *86*, 1021–1035. [CrossRef]
7. Cuadrat, A.; Abad, A.; García-Labiano, F.; Gayán, P.; de Diego, L.; Adánez, J. The use of ilmenite as oxygen-carrier in a 500 Wth Chemical-Looping Coal Combustion unit. *Int. J. Greenh. Gas Control* **2011**, *5*, 1630–1642. [CrossRef]
8. Abdu, Y.A.; Inambao, F.L.; JHassan, A.S.; Nura, S.S.; Karthickeyan, V. Comparative study on pyrolysis and combustion behavior of untreated Matooke biomass wastes in East Africa via TGA, SEM, and EDXS. *Int. J. Energy Environ. Eng.* **2020**, *11*, 265–273.
9. Leion, H.; Mattisson, T.; Lyngfelt, A. Solid fuels in chemical-looping combustion. *Int. J. Greenh. Gas Control* **2008**, *2*, 180–193. [CrossRef]
10. Korus, A.; Klimanek, A.; Sładek, S.; Szlęk, A.; Tilland, A.; Bertholin, S.; Haugen, N.E.L. Kinetic parameters of petroleum coke gasification for modelling chemical-looping combustion systems. *Energy* **2021**, *232*, 120935. [CrossRef]
11. Shen, L.; Wu, J.; Xiao, J.; Song, Q.; Xiao, R. Chemical-Looping Combustion of Biomass in a 10 kWth Reactor with Iron Oxide As an Oxygen Carrier. *Energy Fuels* **2009**, *23*, 2498–2505. [CrossRef]

12. Moldenhauer, P.; Rydén, M.; Mattisson, T.; Jamal, A.; Lyngfelt, A. Chemical-looping combustion with heavy liquid fuels in a 10 kW pilot plant. *Fuel Process. Technol.* **2017**, *156*, 124–137. [CrossRef]
13. Mahalatkar, K.; Kuhlman, J.; Huckaby, E.D.; O'Brien, T. CFD simulation of a chemical-looping fuel reactor utilizing solid fuel. *Chem. Eng. Sci.* **2011**, *66*, 3617–3627. [CrossRef]
14. Yu, H.; Zhang, H.; Buahom, P.; Liu, J.; Xia, X.; Park, C.B. Prediction of thermal conductivity of micro/nano porous dielectric materials: Theoretical model and impact factors. *Energy* **2021**, *233*, 121140. [CrossRef]
15. Wang, X.; Shao, Y.; Jin, B. Thermodynamic Evaluation and Modelling of an Auto-thermal Hybrid System of Chemical Looping Combustion and Air Separation for Power Generation Coupling with CO_2 Cycles. *Energy* **2021**, *236*, 121431. [CrossRef]
16. Wang, X.; Jin, B.; Zhang, Y.; Zhang, Y.; Liu, X. Three Dimensional Modeling of a Coal-Fired Chemical Looping Combustion Process in the Circulating Fluidized Bed Fuel Reactor. *Energy Fuels* **2013**, *27*, 2173–2184. [CrossRef]
17. Wang, S.; Chen, J.; Lu, H.; Liu, G.; Sun, L. Multi-scale simulation of chemical looping combustion in dual circulating fluidized bed. *Appl. Energy* **2015**, *155*, 719–727. [CrossRef]
18. Chen, L.; Yang, X.; Li, G.; Li, X.; Snape, C. Prediction of bubble fluidisation during chemical looping combustion using CFD simulation. *Comput. Chem. Eng.* **2017**, *99*, 82–95. [CrossRef]
19. Luo, H.; Lin, W.; Song, W.; Li, S.; Dam-Johansen, K.; Wu, H. Three dimensional full-loop CFD simulation of hydrodynamics in a pilot-scale dual fluidized bed system for biomass gasification. *Fuel Process. Technol.* **2019**, *195*, 106146. [CrossRef]
20. Parker, J.M. CFD model for the simulation of chemical looping combustion. *Powder Technol.* **2014**, *265*, 47–53. [CrossRef]
21. Kong, D.; Zhou, M.; Wang, S.; Luo, K.; Li, D.; Fan, J. Eulerian-Lagrangian simulation of chemical looping combustion with wide particle size distributions. *Chem. Eng. Sci.* **2021**, *245*, 116849. [CrossRef]
22. Lin, J.; Luo, K.; Hu, C.; Sun, L.; Fan, J. Full-loop simulation of a 1 MWth pilot-scale chemical looping combustion system. *Chem. Eng. Sci.* **2022**, *249*, 117301. [CrossRef]
23. García-Labiano, F.; de Diego, L.F.; Gayán, P.; Abad, A.; Adánez, J. Fuel reactor modelling in chemical-looping combustion of coal: 2—Simulation and optimization. *Chem. Eng. Sci.* **2013**, *87*, 173–182. [CrossRef]
24. Menon, K.G.; Patnaikuni, V.S. CFD simulation of fuel reactor for chemical looping combustion of Indian coal. *Fuel* **2017**, *203*, 90–101. [CrossRef]
25. Shuai, W.; Yunchao, Y.; Huilin, L.; Jiaxing, W.; Pengfei, X.; Guodong, L. Hydrodynamic simulation of fuel-reactor in chemical looping combustion process. *Chem. Eng. Res. Des.* **2011**, *89*, 1501–1510. [CrossRef]
26. May, J.; Alobaid, F.; Ohlemüller, P.; Stroh, A.; Ströhle, J.; Epple, B. Reactive two–fluid model for chemical–looping combustion—Simulation of fuel and air reactors. *Int. J. Greenh. Gas Control* **2018**, *76*, 175–192. [CrossRef]
27. Li, S.; Shen, Y. CFD study of nonuniformity of gas-solid flow through a chemical looping combustion system with symmetrical series loops. *Powder Technol.* **2021**, *387*, 108–124. [CrossRef]
28. Kong, D.; Wang, S.; Luo, K.; Hu, C.; Li, D.; Fan, J. Three-dimensional simulation of biomass gasification in a full-loop pilot-scale dual fluidized bed with complex geometric structure. *Renew. Energy* **2020**, *157*, 466–481. [CrossRef]
29. Lin, J.; Sun, L.; Luo, K.; Kong, D.; Fan, J. Three-dimensional simulation of a gas-fueled chemical looping combustion system with dual circulating fluidized bed reactors. *Energy* **2022**, *246*, 123293. [CrossRef]
30. Abad, A.; Adánez, J.; Cuadrat, A.; García-Labiano, F.; Gayán, P.; de Diego, L.F. Kinetics of redox reactions of ilmenite for chemical-looping combustion. *Chem. Eng. Sci.* **2011**, *66*, 689–702. [CrossRef]
31. Donskoi, E.; Mcelwain, S.; Wibberley, L. Estimation and modeling of parameters for direct reduction in iron ore/coal composites: Part II. Kinetic parameters. *Metall. Mater. Trans. B* **2003**, *34*, 255–266. [CrossRef]
32. Gerber, S.; Behrendt, F.; Oevermann, M. An Eulerian modeling approach of wood gasification in a bubbling fluidized bed reactor using char as bed material. *Fuel* **2010**, *89*, 2903–2917. [CrossRef]
33. Johansson, E.; Lyngfelt, A.; Mattisson, T.; Johnsson, F. Gas leakage measurements in a cold model of an interconnected fluidized bed for chemical-looping combustion. *Powder Technol.* **2003**, *134*, 210–217. [CrossRef]
34. Guan, Y.; Chang, J.; Zhang, K.; Wang, B.; Sun, Q. Three-dimensional CFD simulation of hydrodynamics in an interconnected fluidized bed for chemical looping combustion. *Powder Technol.* **2014**, *268*, 316–328. [CrossRef]
35. Kong, D.; Wang, S.; Zhou, M.; Luo, K.; Hu, C.; Li, D.; Fan, J. Three-dimensional full-loop numerical simulation of co-combustion of coal and refuse derived fuel in a pilot-scale circulating fluidized bed boiler. *Chem. Eng. Sci.* **2020**, *220*, 115612. [CrossRef]
36. Ohlemüller, P.; Reitz, M.; Ströhle, J.; Epple, B. Investigation of chemical looping combustion of natural gas at 1 MWth scale. *Proc. Combust. Inst.* **2019**, *37*, 4353–4360. [CrossRef]
37. Zhang, H.; Liu, X.; Hong, H.; Jin, H. Characteristics of a 10 kW honeycomb reactor for natural gas fueled chemical-looping combustion. *Appl. Energy* **2018**, *213*, 285–292. [CrossRef]
38. Pérez-Vega, R.; Abad, A.; García-Labiano, F.; Gayán, P.; de Diego, L.F.; Adánez, J. Coal combustion in a 50 kWth Chemical Looping Combustion unit: Seeking operating conditions to maximize CO_2 capture and combustion efficiency. *Int. J. Greenh. Gas Control* **2016**, *50*, 80–92. [CrossRef]
39. Li, Y.; Luo, C.; Su, Q. Cold start-up study of methanol reformer based on chemical-looping combustion. *Fuel* **2022**, *317*, 122850. [CrossRef]